Title
Computational and Experimental Investigations of Na-Ion Conduction in Cubic Na3PSe4

Journal
Chemistry of Materials, 28(1)

ISSN
0897-4756

Authors
Bo, Shou-Hang
Wang, Yan
Kim, Jae Chul
et al.

Publication Date
2016-01-12

DOI
10.1021/acs.chemmater.5b04013

Peer reviewed

Title:
Computational and Experimental Investigations of Na-Ion Conduction in Cubic Na<inf>3</inf>PSe<inf>4</inf>

Author:
Bo, SH
Wang, Y
Kim, JC
Richards, WD
Ceder, G

Publication Date:
01-12-2016

Series:
Recent Work

Also Available:
UC Berkeley Previously Published Works

Permalink:
http://escholarship.org/uc/item/02n982wh

DOI:
https://doi.org/10.1021/acs.chemmater.5b04013

Local Identifier(s):
UCPMS ID: 1580903

Abstract:
© 2015 American Chemical Society. All-solid-state Na-ion batteries that operate at or close to room temperature are a promising next-generation battery technology with enhanced safety and reduced manufacturing cost. An indispensable component of this technology is the solid-state electrolyte that allows rapid shuttling of the mobile cation (i.e., Na +) between the cathode and anode. However, there are very few fast Na-ion conductors with ionic conductivity approaching that of the liquid counterparts (i.e., 1 mS cm -1). In this work, we present the synthesis and characterization of a fast Na-ion conductor, cubic Na 3 PSe 4 . This material possesses a room-temperature ionic conductivity exceeding 0.1 mS cm -1 and does not require high-temperature sintering to minimize grain boundary resistance, making it a promising solid-state electrolyte candidate for all-solid-state Na-ion battery applications. On the basis of density functional theory, nudged elastic band, and molecular dynamics investigations, we demonstrate that the framework

of cubic Na 3 PSe 4 only permits rapid Na + diffusion with the presence of defects, and that the formation of the Na vacancy (charge-balanced by slight Se 2- oxidation) is more energetically favorable among the various defects considered. This finding provides important guidelines to further improve Na-ion conduct ivity in this class of materials.

Computational and experimental investigations of Na-ion conduction in cubic Na_3PSe_4

Shou-Hang Bo[a,b], Yan Wang[a], Jae Chul Kim[a], William Davidson Richards[a] and Gerbrand Ceder[a,b,c*]

[a] Department of Materials Science and Engineering, Massachusetts Institute of Technology, Cambridge, MA 02139, United States

[b] Materials Science Division, Lawrence Berkeley National Laboratory, Berkeley, CA 94720, United States

[c] Department of Materials Science and Engineering, University of California, Berkeley, CA 94720, United States

Abstract: All-solid-state Na-ion batteries that operate at or close to room temperature are a promising next-generation battery technology with enhanced safety and reduced manufacturing cost. An indispensable component of this technology is the solid state electrolyte that allows rapid shuttling of the mobile cation (*i.e.*, Na^+) between the cathode and anode. However, there are very few fast Na-ion conductors with ionic conductivity approaching that of the liquid counterparts (*i.e.*, 1 mS cm^{-1}). In this work, we present the synthesis and characterization of a fast Na-ion conductor, cubic Na_3PSe_4. This material possesses a room-temperature ionic conductivity exceeding 0.1 mS cm^{-1}, and does not require high temperature sintering to minimize grain boundary resistance, making it a promising solid-state electrolyte candidate for all-solid-state Na-ion battery applications. Based on density functional theory, nudged elastic band and molecular dynamics investigations, we demonstrate that the framework of cubic Na_3PSe_4 only permits rapid Na^+ diffusion with the presence of defects, and that the formation of the Na vacancy (charge balanced by slight Se^{2-} oxidation) is more energetically favorable among the various defects considered. This finding provides important guidelines to further improve Na-ion conductivity in this class of materials.

Introduction:

High capacity rechargeable batteries play a central role in a variety of emerging technologies, including mobile electronics, plug-in and hybrid electric vehicles, and grid-scale energy storage. Currently, almost all rechargeable batteries utilize liquid electrolytes for the transport of mobile ions between the cathode and anode. However, the liquid electrolyte consists of flammable organic solvents, which can cause fire, dissolve the electrode components (such as the dissolution of polysulfides or polyselenides cathodes in alkaline/S [1-2] and alkaline/Se batteries[3]), or react with the electrodes. All of these issues can, in principle, be resolved by the replacement of the liquid electrolyte with a solid state counterpart.

However, the design and construction of batteries employing only solid state components (*i.e.*, solid-state electrolyte and electrodes) that can rival the performance of liquid electrolyte based batteries is challenging. Despite intensive global research efforts in the past decades, especially in the Li-ion solid-state battery field, a number of issues are still present, including low ionic conductivity and limited voltage stability of solid state electrolyte candidates, as well as interfacial incompatibility between the electrode and the solid state electrolyte[4-25]. These practical issues tie closely with the lack of available solid state electrolyte candidates and fundamental design principles for new solid-state electrolyte discovery.

Compared with all-solid-state rechargeable Li-ion batteries, the development of all-solid-state rechargeable Na-ion batteries provides a potentially more economic alternative to power large-scale devices. However, the research progress in this regard is lagging, mostly due to the lack of fast Na-ion conductors[26-42]. Currently, β- and β"-alumina[28-29], NASICON[26-27], and cubic-Na_3PS_4[30] are the only three inorganic materials which possess Na-ion conductivity comparable to

liquid electrolytes. The two oxides (*i.e.*, β-, β"-alumina and NASICON) exhibit large grain boundary resistance upon room-temperature pressing (or cold pressing), and, therefore, require a high temperature sintering process above approximately 1000 °C to eliminate the grain boundary contribution in the total resistance. This high temperature sintering process, poses a challenge in the fabrication of the solid-state battery, since almost all cathode materials will either decompose or react with the electrolyte at the required temperatures. Sulfides (*e.g.*, Na_3PS_4), on the other hand, can deform easily under mechanical pressure, which allows the production of a dense pellet *via* cold-pressing only [14]. A major drawback of the sulfide based materials is the reduced voltage stability window compared with oxides [4]. However, it is important to note that the stability of the battery is largely controlled by the property of the interfaces between the electrolyte and the electrodes, and is not entirely determined by the absolute voltage stability of the electrolyte. A passivating solid electrolyte interface which permits the transport of the mobile ions [17, 43-44], such as those formed during the decomposition of carbonate solvents in all commercially available rechargeable batteries, can still offer an extended cycle life for the batteries [45-46].

To date, cubic-Na_3PS_4 is the only reported inorganic solid state electrolyte that can be successfully employed in a room-temperature solid state rechargeable Na-ion battery [30]. Na_3PS_4 was first synthesized, structurally and electrochemically characterized in 1992 by Jansen and coworkers [31]. Three polymorphs have been identified for Na_3PS_4 through variable-temperature diffraction and impedance measurements: a room-temperature tetragonal phase, and two unknown high-temperature cubic phases. The tetragonal phase was reported to crystallize in the *P-42$_1$c* space group (# 114) with lattice parameters of $a = b = 6.9520(4)$ Å and $c = 7.0457(5)$ Å. This structure is built with PS_4^{3-} tetrahedra forming a slightly distorted *body-centered-cubic* (*bcc*)

arrangement, and the Na cations filling the skewed octahedral and tetrahedral cavities formed by the S^{2-} anions. The room-temperature Na-ion conductivity of the tetragonal phase was reported to be low (~4 x 10^{-6} S/cm), but the room-temperature conductivity of the two cubic phases were projected to be high based on the extrapolation of high temperature conductivity data. One of the cubic Na_3PS_4 phases was successfully stabilized at room-temperature in the subsequent work performed by Hayashi and coworkers in 2012 [30]. The room-temperature ionic conductivity of this cubic phase was observed to be 0.2 mS/cm with an activation barrier of 27 kJ mol^{-1}. The authors attributed the stabilization of the cubic phase to a high-energy mechanical milling process. In later work performed by the same group, the structure of this cubic phase was determined from laboratory powder X-ray diffraction [40]. It was observed that the structure of the cubic Na_3PS_4 only slightly differs from the tetragonal phase, as half of the PS_4^{3-} tehrahedra are rotated by less than 1° to align all PS_4 tetrahedra along the [111] lattice direction of the cubic structure. The Na ions in this structure are distributed to occupy two distorted tetrahedral sites instead of one tetrahedral and one octahedral site in the tetragonal polymorph.

The substantially higher ionic conductivity and lower activation barrier for Na^+ diffusion in the cubic polymorph, as compared to the tetragonal phase, can be rationalized on the basis of their structural difference. As suggested in a very recent paper, a diffusion path that consists of percolating face-shared tetrahedral sites is generally associated with a low activation barrier, a criterion satisfied by the cubic but not the tetragonal polymorph [47]. It is, however, not yet clear why the cubic phase does not transform into the thermodynamically stable tetragonal polymorph upon cooling from the synthesis temperature of 270 °C, since the subtle rotation of the PS_4^{3-} tetrahedra and the re-distribution of Na-ion in this fast Na-ion conductor are expected to be facile.

Compared to oxides and sulfides, selenides form a huge unexplored chemical space for fast ionic conductor discovery. While the Pearson's crystal structure database contains over 80000 entries of O-based compounds, only approximately 10000 and 6000 entries are found for S- and Se-based compounds, respectively. Also of note is the remarkable success that has been achieved for sulfide-based fast Li-ion conductors[12, 23]. We hypothesize, based upon ionic size considerations, that selenide-based compounds may provide a more suitable structural framework for the rapid diffusion of the much larger Na^+ cations compared with Li^+. This consideration led us to an extensive search of fast Na-ion conductors in the Se-based chemical space *via* high-throughput computational screening, and has identified cubic-Na_3PSe_4 as one of the most promising candidates.

In this work, we report the synthesis of cubic-Na_3PSe_4 as a fast Na-ion conductor. The structure of Na_3PSe_4 was determined from high-resolution synchrotron X-ray diffraction data. The ionic conductivity and activation barrier for Na-ion diffusion were determined through impedance spectroscopy. We demonstrate that cubic-Na_3PSe_4 is a fast Na-ion conductor with a room-temperature ionic conductivity exceeding 0.1 mS/cm, and a low activation energy of 27(1) kJ mol^{-1} for Na^+ diffusion. Also, *ab-initio* calculations suggest that the key to achieve fast Na-ion diffusion in Na_3PSe_4 is the presence of defects.

Results:

Cubic vs. tetragonal: thermodynamic considerations

To investigate the possibility of synthesizing cubic Na_3PSe_4, we have evaluated the energetics of the cubic (*I-43m*, #217), and tetragonal (*P-42$_1$c*, #114) Na_3PSe_4 through density functional theory (DFT) calculations (Table 1). The energy of the cubic structure was calculated to be only 0.8 meV/atom higher than the tetragonal structure, which is well within the error of DFT calculations. We have, therefore, concluded that (1) Na_3PSe_4 can be experimentally synthesized; and (2) the thermodynamically stable form of Na_3PSe_4 at the synthesis temperature (573 K) can be either the tetragonal or cubic polymorph depending on the relative entropy contributions of these two structures. The subtle energy difference, together with the very similar lattice dimensions, between the tetragonal and cubic polymorphs also indicate the possibility of forming complex defects as a result of coexisting tetragonal-like and cubic-like domains, adding another level of complexity to the structure of Na_3PSe_4.

Table 1. *Ab initio* computed phase stability for Na_3PSe_4 in the cubic and tetragonal forms at 0 K.

Structure type of Na_3PSe_4	Energy above the hull
Cubic	0.8 meV/atom
Tetragonal	0.0 meV/atom

Synthesis and structural characterization of cubic Na_3PSe_4

The synthesis of Na_3PSe_4 was performed in a boron nitride tube at a synthesis temperature of 300 °C under a continuous flow of dry Argon gas. We chose boron nitride tube for the synthesis, since B^{3+} and N^{3-} ions are unlikely to be incorporated into the Na_3PSe_4 lattice based on ionic size and coordination preference considerations. As is shown in the Rietveld fitting of the synchrotron X-ray diffraction data as obtained for the as-prepared Na_3PSe_4, the diffraction pattern can be modeled very well with a cubic lattice of $a = b = c = 7.31359(1)$ Å and space group of *I-43m* (#217). The high-quality diffraction data exhibits excellent counting statistics even at a *d*-spacing of ~0.6 Å, allowing an accurate structural determination of this compound. Having good counting statistics at low *d*-spacing is particularly important to independently refine the occupancies and thermal parameters of the crystallographic sites, because these two types of parameters are strongly correlated, and are difficult to decouple by only fitting data at large *d*-spacing. The structural parameters of the as-prepared Na_3PSe_4 as determined from the Rietveld refinement of the synchrotron X-ray diffraction data are presented in Tables S1-3 of the supporting information. It is of interest to note that the thermal parameter (which often reflects the magnitude of the thermal vibration) of the Na site is large (5.2 $Å^2$). This implies that Na cations in the structural framework can be mobile. We also notice that the Na_3PSe_4 structure is isostructural to Na_3SbS_4 [48], which may be related to the similar sizes of the SbS_4^{3-} and PSe_4^{3-} tetrahedral groups. This result implies a possible ionic size matching rule for the design of new materials that adopt the same framework, and indicates that Na_3SbS_4 might be another fast Na-ion conductor. A small amount of unknown impurity was also observed from this high-resolution diffraction data (*e.g.*, extra peaks are observed at 2θ of ~ 7°). The production of trace amounts of impurities might be related to the low melting/boiling points of the precursors (the melting point

and boiling point for Se are 221 °C and 685 °C, respectively, and the boiling point for red phosphorus is 431 °C), which can drive the system to slightly off-stoichiometry at the synthesis temperature of 300 °C. An optimized synthesis, therefore, may require the reaction to be performed in a perfectly sealed system.

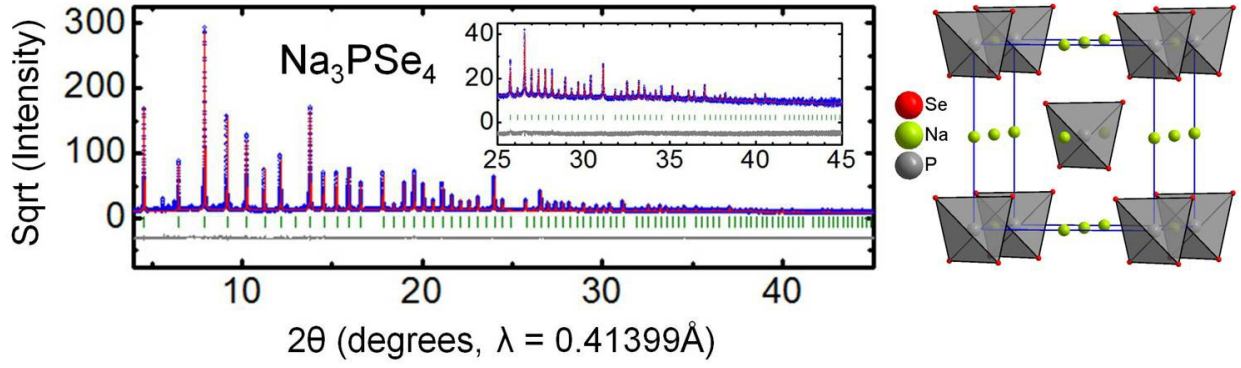

Figure 1. Rietveld fitting of the diffraction pattern for the as-prepared Na_3PSe_4 is shown on the left, with the observation, calculation and difference curves displayed in blue, red and dark grey, respectively. Tick marks corresponding to the Na_3PSe_4 lattice (*I-43m*) are shown in olive. The square root of intensity is displayed on the *y* axis. The refined structure is shown on the right.

Na^+ conductivity and diffusion barrier by impedance spectroscopy

Na^+ conductivity in cubic Na_3PSe_4 was evaluated through impedance spectroscopy at selected temperatures under Argon. The pellets for impedance measurements were fabricated through room-temperature pressing at a pressure of approximately 380 MPa (equivalent to 1.2 metric tons on a 1/4 inch-diameter pellet), without any additional sintering. We collected impedance data during both the heating and cooling cycles, and diffraction data before and after

the impedance measurements, to confirm that no other side reactions or irreversible changes had occurred to the sample (Fig. 2a and 2b). Indeed, the diffraction patterns for the Na_3PSe_4 powder sample before and after the variable-temperature impedance measurements (Fig. 2a) remain almost the same, except for the presence of diffraction peaks corresponding to the indium metal which was pressed onto the pellet as a blocking electrode and which cannot be separated from the Na_3PSe_4 sample. We observed a slight yet noticeable peak width increase for the diffraction pattern of the Na_3PSe_4 powder after impedance measurements compared with the pristine powder. Based on a full-profile fitting, this increased peak width is primarily due to an increase in strain, suggesting there is an irreversible strain development during the mechanical pressing process. This phenomenon appears to be unique for the soft selenide, as it is not often observed in the hard oxides. It is not yet clear as what the physical nature of the strain is and how the strain development impacts the ionic diffusion process.

As is shown in Fig. 2b, the impedance spectra of cubic Na_3PSe_4 consist of a high-frequency semicircle which can be attributed to the response from the Na^+ bulk diffusion process. Fitting of this semicircle with a parallel circuit connection of a resistor and a constant phase element allows us to derive the ionic conductivity. Cubic Na_3PSe_4 exhibits an ionic conductivity of 0.11 mS/cm at 25 °C. This value is comparable with the recently reported Na-ion conductor, cubic-Na_3PS_4 [30], making cubic Na_3PSe_4 one of the two inorganic solid state materials (Na_3PS_4 and Na_3PSe_4) that can deliver a room-temperature ionic conductivity exceeding 0.1 mS/cm with cold pressing only. This property offers significant advantage for utilizing Na_3PSe_4 as a solid state electrolyte in all-solid-state batteries, since cold pressing eliminates the possibility of side reactions that often occur in a high-temperature sintering process. The activation barrier for Na^+ diffusion in Na_3PSe_4 is estimated by plotting the conductivity (σ) as a function of temperature. As

is shown in Fig. 2c, Na_3PSe_4 exhibits a typical Arrhenius-type behavior, as log(σ) linearly correlates with 1/T. The activation barrier for Na^+ diffusion derived from the slope is only 27(1) kJ mol^{-1}, which is almost identical to that of cubic-Na_3PS_4 [30] and is only marginally higher than that of the fastest room-temperature alkaline ion conductor $Li_{10}GeP_2S_{12}$ (24 kJ/mol) [12].

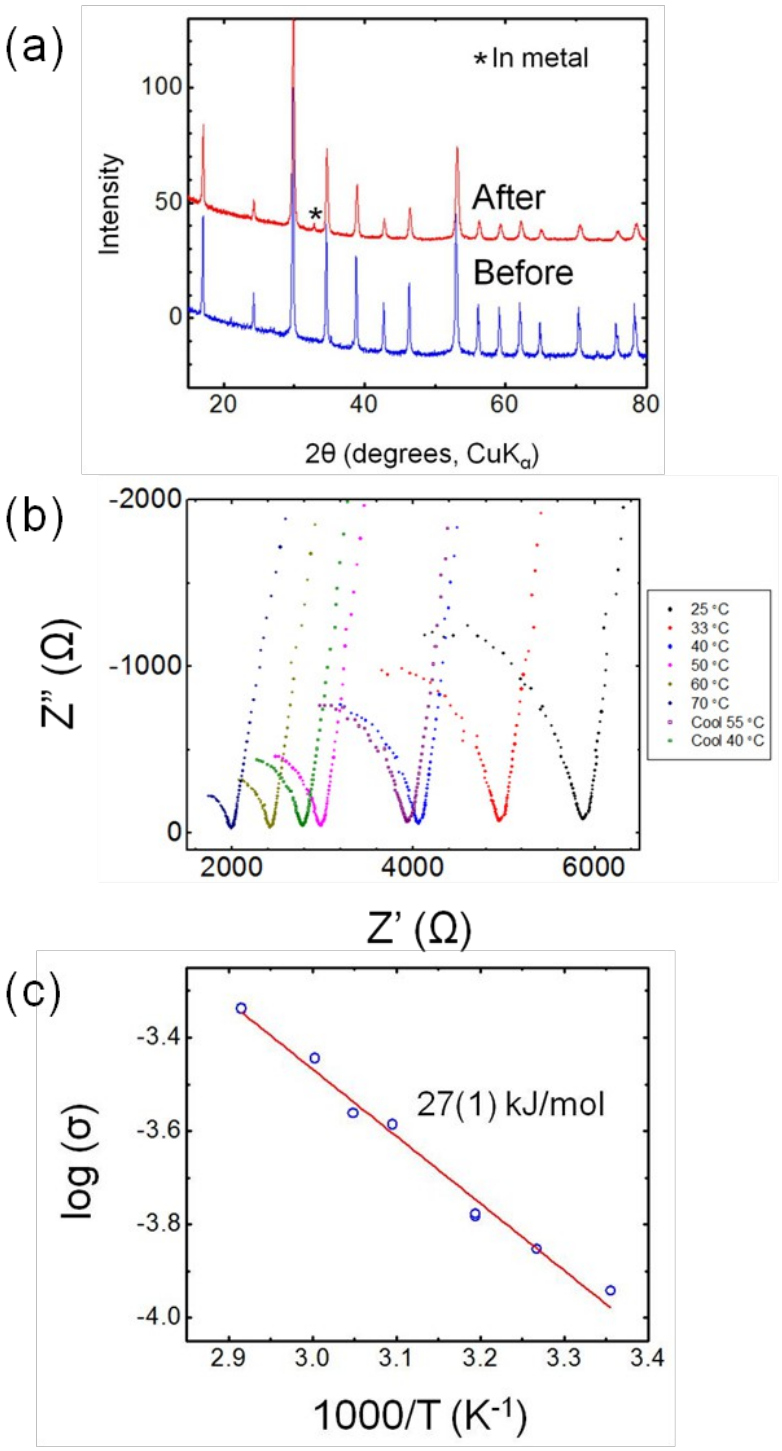

Figure 2. (a) Laboratory X-ray diffraction patterns of Na_3PSe_4 before and after the variable temperature impedance measurements. The peak corresponding to In metal is marked with an asterisk. (b) Impedance spectra of Na_3PSe_4 at various temperatures, with the real and imaginary

parts displayed on the *x* and *y* axes, respectively. (c) Conductivity (S cm^{-1}) vs. temperature (K) plot exhibiting an Arrhenius behavior with an activation barrier of 27 kJ/mol.

Discussion:

Vacancy driven Na^+ conduction?

A fundamental understanding of the Na^+ diffusion process in Na_3PSe_4 can provide important guidelines for future materials optimizations. We have, therefore, performed a theoretical investigation into the Na^+ conduction mechanism in Na_3PSe_4 based on *ab-initio* density functional theory (DFT), because theoretical modeling can provide valuable insights into the atomic scale processes that are not easily accessible by experiments. We, herein, summarize the key findings from this modeling study.

As the Rietveld refinement did not detect any substantial presence of Na vacancies or interstial Na in the as-prepared Na_3PSe_4, the activation barrier for Na diffusion was initially evaluated assuming a perfect Na_3PSe_4 structure. Surprisingly, the *ab-initio* molecular dynamics simulation (AIMD) for stoichiometric Na_3PSe_4 yielded negligible diffusivity for Na ions even at the elevated temperature of 900 K with a simulation period of 120 picoseconds, indicating that the prefect Na_3PSe_4 is not a fast Na-ion conductor at all. However, when a small amount of Na vacancies or interstitial Na was introduced (*i.e.*, 2.1%, which is close to the detection limit of diffraction measurements), Na^+ diffusion became extremely facile. On the basis of AIMD simulations at elevated temperatures, the activation barrier for Na^+ diffusion with the presence of 2.1% Na vacancies was determined to be 11 kJ mol^{-1} (Fig. S1) and the extrapolated room temperature (300 K) conductivity is 28.9 mS/cm. We chose the Na vacancy defect in our

calculations, because it possesses the lowest formation energy among the various defects investigated (discussed more below). The small activation energy is further confirmed by a nudged elastic band calculation of the Na vacancy migration barrier at 0 K (approximately 5 kJ mol^{-1} as shown in Fig. 3). These results suggest that the cubic Na_3PSe_4 structural framework is indeed very well-suited for Na^+ diffusion, but the key for fast Na^+ diffusion to occur is the presence of defects. We note a very recent work on cubic Na_3PSe_4 with a reported room-temperature conductivity of 1 mS cm^{-1} [49]. This work used different precursors and reaction vessels compared to our work, and also included an additional ball milling step before the impedance measurements. All of these may cause an increase in defect concentration, and the resulting increase in ionic conductivity compared to the current work, consistent with our defect-driven diffusion mechanism.

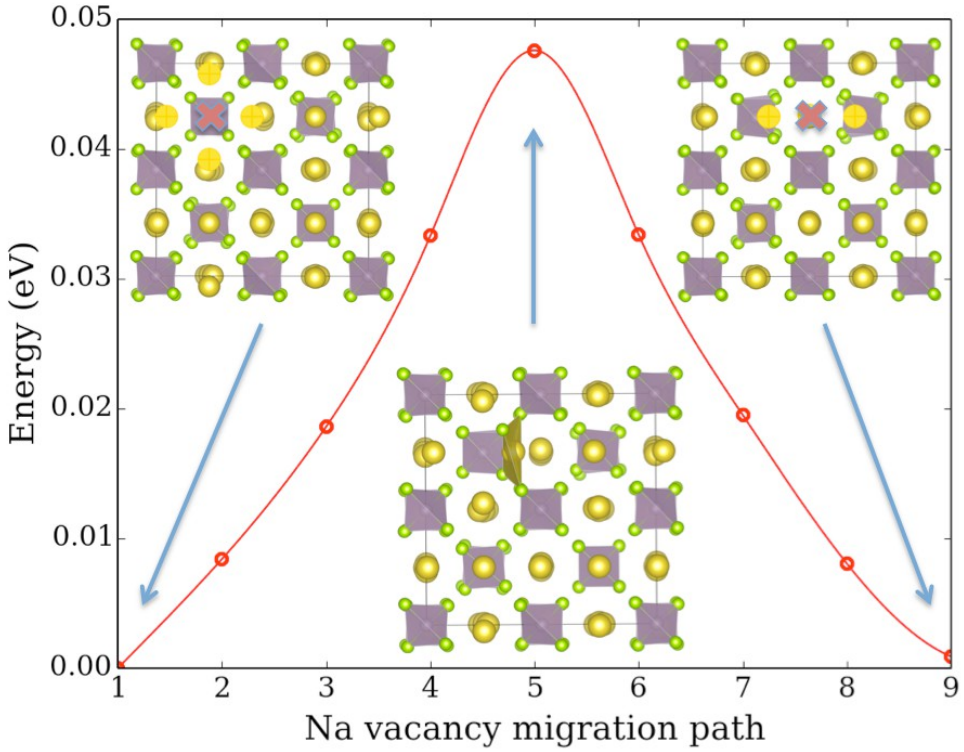

Figure 3: Calculated Na vacancy migration barrier in the cubic Na_3PSe_4. The insets show the structure of the initial state (top left), transition state (bottom middle) and the final state (top right). The Na atoms, Se atoms and PSe_4 tetrahedra are colored yellow, green and purple, respectively. In both the initial state and the final state, four Na ions (highlighted, only two are shown in the final state) surrounding the Na vacancy site (marked as a red cross) are slightly displaced from their original positions in the pristine Na_3PSe_4 towards the vacancy site. In the transition state, the migration Na ion is in a distorted tetrahedral site (the $NaSe_4$ tetrahedra colored as yellow).

To investigate which type of defect is more likely to be present in the synthesized Na_3PSe_4, we have calculated the formation energies for a series of different defects (*i.e.*, Na vacancy, interstitial Na, Frenkel defect, and aliovalent ion substitution for both Na and P cations). The selection of aliovalent dopants was based on the common contamination which may occur in the synthesis, such as the use of alumina crucibles, quartz tubes and zirconia ball mill jars. The calculated defect formation energies are listed in Table 2, and the chemical potentials used in these calculations are presented in Table S4. The Na vacancy formation energy of approximately 0.39 eV is the lowest among all the defects investigated, and the formation energies of all the other defects are substantially larger (*i.e.*, 0.5 to 4 eV larger than that of the vacancy formation energy). Based on an analysis of the DFT relaxed structure containing the Na vacancy as well as integrated electron densities for all atoms, we believe the Na vacancy defect is stabilized through two mechanisms: (1) the displacement of the neighboring Na ions toward the vacant site, minimizing Columbic repulsion between the four adjacent Na ions near the vacancy (Fig. 3); and (2) a partial oxidation of Se^{2-}. The charge analysis on the simulated structures of pristine Na_3PSe_4

and defect Na_3PSe_4 with Na vacancy indicate that the average charge on Se atoms get slightly oxidized after removal of the 2.1 % of Na sites. The partial oxidation of Se^{2+} is delocalized in the defect structure, as the amount of charge difference on each Se atom (Na defect structure versus pristine compound) is very small.

Table 2. Calculated defect energies for Na_3PSe_4. The types of dopants selected were based on the common contamination that may occur in the syntheses. The formation energy of Na vacancy was observed to be substantially lower than any other defects investigated.

Defect type	Composition	Defect energy
Na vacancy	$Na_{47}P_{16}Se_{64}$	0.39 eV
Na interstitial	$Na_{49}P_{16}Se_{64}$	1.78 eV
Frenkel defect (Na vacancy + interstitial pair)	Na_3PSe_4	1.14 eV
Na interstitial with Si^{4+} defect at P^{5+} site	$Na_{49}SiP_{15}Se_{64}$	0.94 eV
Na vacancies with Al^{3+} defect at Na^+ site	$Na_{45}AlP_{16}Se_{64}$	1.33 eV
Na vacancies with Zr^{4+} defect at Na^+ site	$Na_{44}ZrP_{16}Se_{64}$	1.39 eV
P deficiency	$Na_{48}P_{15}Se_{64}$	4.04 eV

We expect that the actual defect formation energy in the cubic Na_3PSe_4 could be lower than 0.39 eV or 37 kJ mol^{-1} at elevated temperatures due to entropic contributions and defect-defect interactions. Taking into account that the experimentally determined activation barrier should be a sum of the ionic migration barrier and the defect formation energy (assuming intrinsic conduction behavior), the theoretically determined diffusion barrier (5 kJ/mol at 0 K)

and Na vacancy formation energy (37 kJ/mol at 0 K) is in reasonable agreement with the experimental observation (27 kJ/mol), indicating that the Na^+ diffusion in Na_3PSe_4 is likely Na-vacancy driven. However, the fact that the experimental activation energy is lower indicates that an extrinsic defect concentration may exist or that more complex defect clusters may be forming. An alternative Na^+ conduction mechanism is based upon the coexistence of tetragonal-like and cubic-like domains (discussed earlier). This type of defect is difficult to be investigated by theory only, and is an opportunity for a detailed structural study on the local scale.

Conclusions:

The Na-ion conduction characteristics of cubic Na_3PSe_4 were investigated experimentally and computationally. This compound exhibits a room-temperature ionic conductivity of 0.11 mS/cm with a low activation barrier of 27(1) kJ/mol. Of particular note is that no high-temperature sintering process is required to achieve such a high ionic conductivity at room temperature, which offers a substantial advantage for the use of Na_3PSe_4 as solid state electrolyte for all-solid-state Na-ion batteries. We also demonstrated through a systematic theoretical study that only defective Na_3PSe_4 allows rapid Na^+ diffusion, providing guidelines for future materials optimizations. This work has two important implications for future studies in related fields: (1) selenide based compounds represent a promising platform for the discovery of new fast Na-ion conductors; and (2) the current study opens up new opportunities for the exploration of Se based battery chemistry, such as the construction of all-solid-state Na/Se battery.

Methods:

Synthesis of Na_3PSe_4: Na_2Se (Alfa Aesar, 99.8%), red phosphorus (Sigma Aldrich, ≥99.99% trace metal basis) and selenium (Sigma Aldrich, 99.99% trace metal basis) powder were mixed with the stoichiometric ratio in an Argon filled glove box. The resulting mixture (~1 g) was then placed into a BN tube (3 mm inner diameter and 4 mm outer diameter), which was wrapped in aluminum foil, with the open end sealed with a stainless steel Swagelok cap (3/8 inch). This tube was transferred into a sealed alumina tube furnace, which was purged with pre-dried Ar gas (oxygen/moisture traps, model MT200-4-D, Agilent). The furnace was quickly ramped to 300 C within ~10 minutes, and was held at the same temperature for 12 h to complete the reaction. During the reaction, a continuous flow of Argon gas with a flow rate of approximately 30 mL min^{-1} was used. Final products were collected after the furnace was naturally cooled down to room temperature, and were transferred immediately into the glove box for further characterizations. The Na_3PSe_4 powder was manually ground and re-heated with the same condition to ensure obtain the final product.

Experimental characterizations: to verify the purity of Na_3PSe_4, X-ray diffraction was performed on a Rigaku Smartlab diffractometer with Cu K_α radiation. Typically, the powder sample was first sealed into a special glass capillary (0.5 mm in diameter, Charles Supper) in the glove box, and was then measured in the diffractometer equipped with a capillary stage. We utilized convergent beam and the 1D silicon strip detector (*i.e.*, D/tex Ultra high speed detector) to improve the signal-to-noise ratio of the diffraction data. For structural determination of Na_3PSe_4, the diffraction data was collected at beamline 11BM at the Advanced Photon Source (APS) of Argonne National Laboratory with a constant wavelength of ~0.41 Å. Due to the air sensitivity of Na_3PSe_4, the as-prepared Na_3PSe_4 powder was packed into a 0.5-mm diameter special glass capillary in an argon glove box. The glass capillary was further secured into a 0.8-

mm diameter Kapton tube. The Rietveld refinements were performed using the TOPAS 4.2 software package (Bruker).

Impedance measurements of Na_3PSe_4 were performed with a Solartron MTS system. The impedance data were collected from 1 MHz to 100 Hz with a *dc* voltage amplitude of 10 mV. To prepare the sample for impedance measurements, approximately 100 mg of Na_3PSe_4 powder was first pressed into a disk-shaped pellet with the use of a 1/4 inch die under a pressure of 1-1.2 metric tons. Indium metal disks (99.999%, Goodfellow Corporation) were then pressed onto both sides of the pellet with a pressure of approximately 0.8 metric tons. The resulting pellet was assembled into a Swagelok cell, using stainless steel rods as current collectors. The Swagelok cell was subsequently sealed into a tube furnace under a continuous flow of Ar for variable temperature impedance measurements. Data were collected from room temperature to 80 °C during both the heating and cooling cycles.

First principles density-functional-theory calculations: density functional theory (DFT) based on the Perdew-Burke-Ernzerhof generalized gradient approximation [50] with interactions between ion cores and valence electrons described by the projector augmented wave method [51] as implemented in the VASP package [52] was employed in the present work. A plane-wave energy cut-off of 520 eV and *k*-point density of at least 500/(number of atoms in the unit cell) was used for total energy calculations.

Thermodynamic stability was evaluated using computed DFT total energies. The stability of any phase was evaluated by comparing its energy to linear combinations of the energy of other phases (leading to the same composition) using the convex hull construction. The stability analysis was performed versus all compounds present in the ICSD database plus our internal

database of structures generated with data-mined substitution rules. The stability was quantified by evaluating the energy above the hull, which represents the magnitude of a compound's decomposition energy. The value of the energy above the hull is non-negative and measures the thermodynamic driving force for the compound to decompose into a set of alternate phases. A thermodynamically stable compound will have an energy above the hull of 0 meV/atom as it is part of the convex hull of stable phases.

Gamma-point only sampling of *k*-space and a plane-wave energy cutoff of 400 eV were used for the *ab-initio* Molecular dynamics (AIMD) simulations. The Na_3PSe_4 supercell consists of 16 formula units. About 2.1% of Na vacancies are introduced in the AIMD simulations (one Na ion is removed from the supercell originally containing 48 Na ions), as stoichiometric Na_3PSe_4 do not show significant Na diffusion. The AIMD simulations were taken on the canonical ensemble and the time step was set to 2 femtosecond. Temperatures were initialized at 100K and elevated to appropriate temperatures (500K, 600 K, 720K, 900 K and 1200 K), and the AIMD simulations were performed with about 160 picosecond for statistical analysis. The Na atomic trajectories were monitored during the simulation, and the diffusivities of Na ions were calculated for determination of the activation energy.

Activation barrier for the Na vacancy migration was calculated using the nudged elastic band method (NEB) [53] in a large supercell comprises 16 formula units to minimize the interaction between the periodic images. A 2 × 2 × 2 *k*-point grid was used and the plane-wave energy cut-off was set to 520 eV for the NEB calculation.

To find the most reasonable defect in the cubic-Na_3PSe_4, structures with possible defects were calculated. For each case, several defect configurations were investigated with a

supercell containing 64 Se atoms, and the lowest defect formation energy was considered. The defect formation energy was calculated as [44]:

$$E_d = E_{pristine} - E_{defect} + \sum_i^N \Delta n_i \mu_i$$

where E_{defect} and $E_{pristine}$ are the total energy of the Na_3PSe_4 supercell with and without the defect, respectively; Δn_i is the number of atoms of element i added to (or removed from) the supercell to create the supercell with the defect, and μ_i is the chemical potential of element i. This was summed for all elements (N) that are added (or removed) during the formation of the defect. The chemical potential for each element i was determined from the multi-phase equilibrium that contains the composition of the defect structure, and was calculated as the slope in the direction of element *i* in the phase diagram. The python materials genomics (pymatgen) open-source library [54] was used to generate the phase diagram and calculate the chemical potentials at the phase equilibrium in which the defected material exists in the phase diagram. To compute the relevant phase diagrams that are needed to obtain the chemical potentials of defect species in the defect energy computations, we obtained relevant structures from the International Crystal Structure Database (ICSD), and from our internal database of structures generated with data-mined substitution rules. All compounds in a given ternary Na−P−Se or quintenary Na−P−Se−M system (where M = dopant, for example, Si, Al and Zr) were calculated.

Acknowledgement:

This work was supported by the Samsung Advanced Institute of Technology. Use of the Advanced Photon Source at Argonne National Laboratory was supported by the U. S.

Department of Energy, Office of Science, Office of Basic Energy Sciences, under Contract No. DE-AC02-06CH11357. Computational resources from the National Energy Research Scientific Computing Center (NERSC), a DOE Office of Science User Facility supported by the Office of Science of the U.S. Department of Energy under Contract No. DE-AC02-05CH11231, and from the Extreme Science and Engineering Discovery Environment (XSEDE, which is supported by National Science Foundation grant number ACI-1053575) are gratefully acknowledged.

Supporting information:

The chemical potentials used in the defect formation calculations, the synchrotron X-ray diffraction data, the input file for Rietveld refinement, the cif file and associated structural information regarding Na_3PSe_4. The supporting information is available free of charge on the ACS publications websites at DOI:XXXXXXXXX.

Corresponding Author:

* Email: gceder@berkeley.edu

References:

1. Bruce, P. G.; Freunberger, S. A.; Hardwick, L. J.; Tarascon, J.-M., Li-O_2 and Li-S batteries with high energy storage. *Nat Mater* **2012,** *11*, 19-29.

2. Ellis, B. L.; Nazar, L. F., Sodium and sodium-ion energy storage batteries. *Curr. Opin. Solid State Mater. Sci.* **2012,** *16*, 168-177.

3. Abouimrane, A.; Dambournet, D.; Chapman, K. W.; Chupas, P. J.; Weng, W.; Amine, K., A new class of lithium and sodium rechargeable batteries based on selenium and selenium–sulfur as a positive electrode. *J Am Chem Soc* **2012,** *134*, 4505-4508.

4. Ong, S. P.; Mo, Y.; Richards, W. D.; Miara, L.; Lee, H. S.; Ceder, G., Phase stability, electrochemical stability and ionic conductivity of the $Li_{10\pm1}MP_2X_{12}$ (M= Ge, Si, Sn, Al or P, and X= O, S or Se) family of superionic conductors. *Energy Environ. Sci.* **2013,** *6*, 148-156.

5. Liang, C. C., Conduction Characteristics of the Lithium Iodide-Aluminum Oxide Solid Electrolytes. *J. Electrochem. Soc.* **1973,** *120*, 1289-1292.

6. Ohta, N.; Takada, K.; Zhang, L.; Ma, R.; Osada, M.; Sasaki, T., Enhancement of the High-Rate Capability of Solid-State Lithium Batteries by Nanoscale Interfacial Modification. *Adv. Mater.* **2006,** *18*, 2226-2229.

7. Sakuda, A.; Hayashi, A.; Tatsumisago, M., Interfacial Observation between $LiCoO_2$ Electrode and $Li_2S-P_2S_5$ Solid Electrolytes of All-Solid-State Lithium Secondary Batteries Using Transmission Electron Microscopy. *Chem. Mater.* **2009,** *22*, 949-956.

8. Ma, C.; Chen, K.; Liang, C.; Nan, C.-W.; Ishikawa, R.; More, K.; Chi, M., Atomic-scale origin of the large grain-boundary resistance in perovskite Li-ion-conducting solid electrolytes. *Energy Environ. Sci.* **2014,** *7*, 1638-1642.

9. Sahu, G.; Lin, Z.; Li, J.; Liu, Z.; Dudney, N.; Liang, C., Air-stable, high-conduction solid electrolytes of arsenic-substituted Li_4SnS_4. *Energy Environ. Sci.* **2014,** *7*, 1053-1058.

10. Thangadurai, V.; Weppner, W., $Li_6ALa_2Ta_2O_{12}$ (A= Sr, Ba): Novel Garnet-Like Oxides for Fast Lithium Ion Conduction. *Adv. Funct. Mater.* **2005,** *15*, 107-112.

11. Haruyama, J.; Sodeyama, K.; Han, L.; Takada, K.; Tateyama, Y., Space–Charge Layer Effect at Interface between Oxide Cathode and Sulfide Electrolyte in All-Solid-State Lithium-Ion Battery. *Chem. Mater.* **2014,** *26*, 4248-4255.

12. Kamaya, N.; Homma, K.; Yamakawa, Y.; Hirayama, M.; Kanno, R.; Yonemura, M.; Kamiyama, T.; Kato, Y.; Hama, S.; Kawamoto, K., A lithium superionic conductor. *Nat. Mater.* **2011,** *10*, 682-686.

13. de La Mora, P.; Goodenough, J. B., Lithiated rare-earth thiospinels and selenospinels. *J Solid State Chem* **1987,** *70*, 121-128.

14. Inaguma, Y.; Liquan, C.; Itoh, M.; Nakamura, T.; Uchida, T.; Ikuta, H.; Wakihara, M., High ionic conductivity in lithium lanthanum titanate. *Solid State Commun.* **1993,** *86*, 689-693.

15. Alpen, U. v.; Rabenau, A.; Talat, G. H., Ionic conductivity in Li_3N single crystals. *Appl. Phys. Lett.* **1977,** *30*, 621-623.

16. Du, F.; Ren, X.; Yang, J.; Liu, J.; Zhang, W., Structures, Thermodynamics, and Li^+ Mobility of $Li_{10}GeP_2S_{12}$: A First-Principles Analysis. *J. Phys. Chem. C* **2014,** *118*, 10590-10595.

17. Mo, Y.; Ong, S. P.; Ceder, G., First principles study of the $Li_{10}GeP_2S_{12}$ lithium super ionic conductor material. *Chem. Mater.* **2011,** *24*, 15-17.

18. Bron, P.; Johansson, S.; Zick, K.; Schmedt auf der Günne, J. r.; Dehnen, S.; Roling, B., $Li_{10}SnP_2S_{12}$: an affordable lithium superionic conductor. *J Am Chem Soc* **2013,** *135*, 15694-15697.

19. Rangasamy, E.; Liu, Z.; Gobet, M.; Pilar, K.; Sahu, G.; Zhou, W.; Wu, H.; Greenbaum, S.; Liang, C., An Iodide-Based $Li_7P_2S_8I$ Superionic Conductor. *J Am Chem Soc* **2015,** *137*, 1384-1387.

20. Murugan, R.; Thangadurai, V.; Weppner, W., Fast Lithium Ion Conduction in Garnet-Type $Li_7La_3Zr_2O_{12}$. *Angew. Chem., Int. Ed.* **2007,** *46*, 7778-7781.

21. Liu, Z.; Fu, W.; Payzant, E. A.; Yu, X.; Wu, Z.; Dudney, N. J.; Kiggans, J.; Hong, K.; Rondinone, A. J.; Liang, C., Anomalous high ionic conductivity of nanoporous β-Li_3PS_4. *J Am Chem Soc* **2013,** *135*, 975-978.

22. Zhao, Y.; Daemen, L. L., Superionic conductivity in lithium-rich anti-perovskites. *J Am Chem Soc* **2012,** *134*, 15042-15047.

23. Deiseroth, H. J.; Kong, S. T.; Eckert, H.; Vannahme, J.; Reiner, C.; Zaiss, T.; Schlosser, M., Li_6PS_5X: A Class of Crystalline Li-Rich Solids With an Unusually High Li^+ Mobility. *Angew. Chem., Int. Ed* **2008,** *47*, 755-758.

24. Li, J.; Ma, C.; Chi, M.; Liang, C.; Dudney, N. J., Solid Electrolyte: the Key for High-Voltage Lithium Batteries. *Adv. Energy Mater.* **2015,** *5*, 1401408

25. Bates, J. B.; Dudney, N. J.; Neudecker, B.; Ueda, A.; Evans, C. D., Thin-film lithium and lithium-ion batteries. *Solid State Ion.* **2000,** *135*, 33-45.

26. Von Alpen, U.; Bell, M. F.; Höfer, H. H., Compositional dependence of the electrochemical and structural parameters in the Nasicon system ($Na_{1+x}Si_xZr_2P_{3-x}O_{12}$). *Solid State Ion.* **1981,** *3*, 215-218.

27. Goodenough, J. B.; Hong, H.-P.; Kafalas, J. A., Fast Na^+-ion transport in skeleton structures. *Mater Res Bull* **1976,** *11*, 203-220.

28. Kummer, J. T., β-alumina electrolytes. *Prog. Solid State Chem.* **1972,** *7*, 141-175.

29. Hooper, A., A study of the electrical properties of single-crystal and polycrystalline β-alumina using complex plane analysis. *J. Phys. D: Appl. Phys.* **1977,** *10*, 1487.

30. Hayashi, A.; Noi, K.; Sakuda, A.; Tatsumisago, M., Superionic glass-ceramic electrolytes for room-temperature rechargeable sodium batteries. *Nat. Commun.* **2012,** *3*, 856.

31. Jansen, M.; Henseler, U., Synthesis, structure determination, and ionic conductivity of sodium tetrathiophosphate. *J Solid State Chem* **1992,** *99*, 110-119.

32. Udovic, T. J.; Matsuo, M.; Unemoto, A.; Verdal, N.; Stavila, V.; Skripov, A. V.; Rush, J. J.; Takamura, H.; Orimo, S.-i., Sodium superionic conduction in $Na_2B_{12}H_{12}$. *Chem. Commun.* **2014,** *50*, 3750-3752.

33. Fergus, J. W., Ion transport in sodium ion conducting solid electrolytes. *Solid State Ion.* **2012,** *227*, 102-112.

34. Kuriakose, A. K.; Wheat, T. A.; Ahmad, A.; Dirocco, J., Synthesis, sintering, and microstructure of NASICONS. *J. Am. Chem. Soc*, **1984,** *67*, 179-183.

35. Hong, H.-P., Crystal structures and crystal chemistry in the system $Na_{1+x}Zr_2Si_xP_{3-x}O_{12}$. *Mater Res Bull* **1976,** *11*, 173-182.

36. Hayashi, A.; Noi, K.; Tanibata, N.; Nagao, M.; Tatsumisago, M., High sodium ion conductivity of glass–ceramic electrolytes with cubic Na_3PS_4. *J. Power Sources* **2014,** *258*, 420-423.

37. Wei, T.; Gong, Y.; Zhao, X.; Huang, K., An All-Ceramic Solid-State Rechargeable Na^+-Battery Operated at Intermediate Temperatures. *Adv. Funct. Mater.* **2014,** *24*, 5380-5384.

38. Kim, S. K.; Mao, A.; Sen, S.; Kim, S., Fast Na-Ion Conduction in a Chalcogenide Glass–Ceramic in the Ternary System Na_2Se–Ga_2Se_3–$GeSe_2$. *Chem. Mater.*, **2014,** *26*, 5695-5699.

39. Tanibata, N.; Noi, K.; Hayashi, A.; Tatsumisago, M., Preparation and characterization of highly sodium ion conducting Na_3PS_4–Na_4SiS_4 solid electrolytes. *Rsc Adv* **2014,** *4*, 17120-17123.

40. Tanibata, N.; Noi, K.; Hayashi, A.; Kitamura, N.; Idemoto, Y.; Tatsumisago, M., X-ray Crystal Structure Analysis of Sodium-Ion Conductivity in 94 Na_3PS_4· 6 Na_4SiS_4 Glass-Ceramic Electrolytes. *Chemelectrochem* **2014,** *1*, 1130-1132.

41. Hibi, Y.; Tanibata, N.; Hayashi, A.; Tatsumisago, M., Preparation of sodium ion conducting Na_3PS_4–NaI glasses by a mechanochemical technique. *Solid State Ion.* **2015,** *270*, 6-9.

42. Tanibata, N.; Hayashi, A.; Tatsumisago, M., Improvement of Rate Performance for All-Solid-State $Na_{15}Sn_4$/Amorphous TiS_3 Cells Using 94Na_3PS_4· 6Na_4SiS_4 Glass-Ceramic Electrolytes. *J. Electrochem. Soc.* **2015,** *162*, A793-A795.

43. Zhu, Y.; He, X.; Mo, Y., Origin of Outstanding Stability in the Lithium Solid Electrolyte Materials: Insights from Thermodynamic Analyses Based on First-Principles Calculations. *Acs Appl Mater Inter* **2015,** *7*, 23685-23693.

44. Miara, L. J.; Suzuki, N.; Richards, W. D.; Wang, Y.; Kim, J. C.; Ceder, G., Li-ion conductivity in Li_9S_3N. *J. Mater. Chem. A* **2015,** *3*, 20338-20344.

45. Winter, M., The solid electrolyte interphase–the most important and the least understood solid electrolyte in rechargeable Li batteries. *Z. Phys. Chem.* **2009,** *223*, 1395-1406.

46. Verma, P.; Maire, P.; Novák, P., A review of the features and analyses of the solid electrolyte interphase in Li-ion batteries. *Electrochim Acta* **2010,** *55*, 6332-6341.

47. Wang, Y.; Richards, W. D.; Ong, S. P.; Miara, L. J.; Kim, J. C.; Mo, Y.; Ceder, G., Design principles for solid-state lithium superionic conductors. *Nat Mater* **2015,** *advance online publication*.

48. Graf, H. A.; Schäfer, H., Zur Strukturchemie der Alkalisalze der Tetrathiosäuren der Elemente der 5. Hauptgruppe. *Zeitschrift für anorganische und allgemeine Chemie* **1976,** *425*, 67-80.

49. Zhang, L.; Yang, K.; Mi, J.; Lu, L.; Zhao, L.; Wang, L.; Li, Y.; Zeng, H., Na_3PSe_4: A Novel Chalcogenide Solid Electrolyte with High Ionic Conductivity. *Adv. Energy Mater.* **2015**.

50. Perdew, J. P.; Burke, K.; Ernzerhof, M., Generalized gradient approximation made simple. *Phys. Rev. Lett.* **1996,** *77*, 3865.

51. Blöchl, P. E., Projector augmented-wave method. *Phys Rev B* **1994,** *50*, 17953.

52. Kresse, G.; Furthmüller, J., Efficient iterative schemes for ab initio total-energy calculations using a plane-wave basis set. *Phys Rev B* **1996,** *54*, 11169.

53. Henkelman, G.; Uberuaga, B. P.; Jónsson, H., A climbing image nudged elastic band method for finding saddle points and minimum energy paths. *J. Chem. Phys.* **2000,** *113*, 9901-9904.

54. Ong, S. P.; Richards, W. D.; Jain, A.; Hautier, G.; Kocher, M.; Cholia, S.; Gunter, D.; Chevrier, V. L.; Persson, K. A.; Ceder, G., Python Materials Genomics (pymatgen): A robust, open-source python library for materials analysis. *Comp Mater Sci* **2013,** *68*, 314-319.

TOC: